Received: 16 January 2025 | Revised: 18 April 2025 | Accepted: 6 May 2025

DOI: 10.1111/jace.20660

Journal of the American Ceramic Society

RESEARCH ARTICLE

# Reliability evaluation scheme for ceramics based on defect size distribution inversely estimated from standardized tests

**Taiyo Maeda**[1] | **Toshio Osada**[2,3] | **Shingo Ozaki**[2,3]

[1]Graduate School of Engineering Science, Yokohama National University, Yokohama, Japan

[2]High-Reliability Heat-Resistant Materials Group, Research Center for Structural Materials, National Institute for Materials Science, Tsukuba, Japan

[3]Division of System Research, Faculty of Engineering, Yokohama National University, Yokohama, Japan

**Correspondence**
Shingo Ozaki, Division of System Research, Faculty of Engineering, Yokohama National University, Yokohama, Japan.
Email: s-ozaki@ynu.ac.jp

**Funding information**
New Energy and Industrial Technology Development Organization, Grant/Award Number: JPNP22005

**Abstract**

Ceramic components fracture stochastically, resulting in scatter and size dependence of the strength. Therefore, the strength properties obtained from a standardized test cannot be directly used to determine the design strength of the arbitrary-shaped components under different boundary conditions for brittle ceramics. In this study, we propose a novel strength evaluation scheme where an inversely analyzed defect distribution is used as a common indicator to evaluate the reliability of brittle ceramic components. First, the defect distribution of the target lot is inversely estimated as a common indicator based on experimental results of the bending strengths using the swarm intelligence optimization method. The scatter of the bending strength tested under different boundary conditions is then predicted using the estimated defect distribution. The analyzed defect distribution was found to be consistent with the observed distribution and can be used to predict other experimental results. The versatility and limitations of the scheme were discussed by examining the selection of a standardized strength test for optimization and the impact of model discretization on the inverse estimation of defect distribution. The results suggest that the proposed scheme can be applied to evaluate the strength scatter of components with arbitrary shapes and under arbitrary boundary conditions.

**KEYWORDS**
defects, extreme value statistics, inverse analysis, strength analysis, Weibull plot

## 1 | INTRODUCTION

Ceramics are used as structural materials in automobile and aircraft engine components because of their light weight and excellent heat and corrosion resistance.[1–5] In recent years, there has been increased research on the additive manufacturing of ceramics and its application to complex-shaped components.[6–11] However, ceramics are brittle and highly susceptible to defects, resulting in scatter and size dependency on the strengths of those components.[12–15] For components of ductile materials such as metals, various strength indices such as ultimate tensile strength and 0.2% proof stress (or yield stress) obtained from "standardized tests" can be directly applied to the reliability design of components under actual working loads. By contrast, this conventional reliability design scheme is not applicable to components of brittle materials. The strengths of ceramic components of

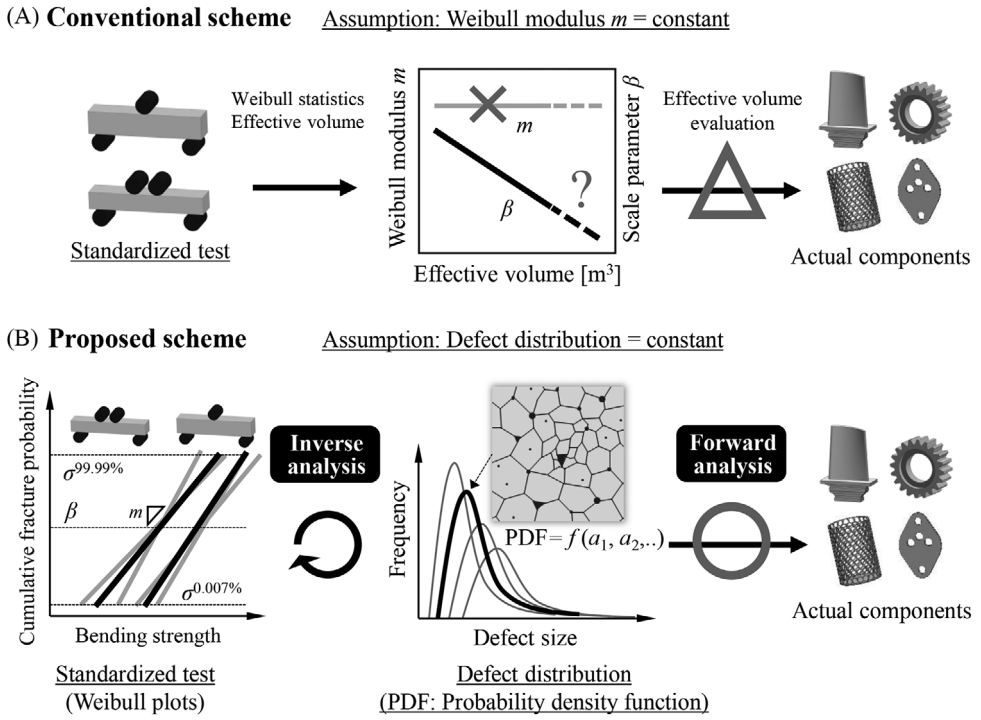


**FIGURE 1** Schematics of strength evaluation schemes for ceramic components: (A) conventional scheme, (B) proposed scheme.

different sizes and shapes can also be evaluated to some extent using Weibull statistics and the concept of effective volume (Figure 1A), assuming that the Weibull modulus $m$, a statistical material constant, is constant regardless of the effective volume.[14,16–19] However, since the Weibull modulus shows a large deviation depending on the number of test specimens,[14,15,20] it is difficult to determine the true value of $m$ with a realistic number of tests. Furthermore, since the $m$-values can vary depending on effective volume,[14,15] the assumption that $m$ = constant in Weibull's size effect law cannot hold. In addition, it is difficult to evaluate the effective volume of a complex-shaped component under actual load conditions, and the strength index estimated based on Weibull's size effect law does not always guarantee the reliability of components as shown in Figure 1A. From a cost standpoint, evaluating the strength reliability of target components using strength tests with many components under service conditions is not realistic. Thus, novel strategies are required to correlate the results of standardized strength tests with the strength evaluation of components to advance the reliable design of ceramics.

Ozaki et al.[15,21–23] proposed a numerical simulation method for alumina fine ceramics to predict the scatter of the bulk strength of a component from microstructural information, such as the distribution of pore size, pore aspect ratio, and grain size (referred to as "forward analysis" in this study). These studies predict the bulk strength scatter based on defect distribution data obtained from microstructural observations of the target material and also the strength scatter under multiple test conditions.[15,22] Various studies have reported a strong correlation between strength scatter in ceramics and the distribution of defects generated in the manufacturing process.[12–15,17–19,21–31] In particular, Andreasen reported the prediction method of fracture statistics for components with diverse shapes and boundary conditions by correlating Weibull distributions based on test results with extreme value statistical distributions of crack sizes.[18] Cook and DelRio reported attempts to estimate flaw populations from strength test results and demonstrated its effectiveness.[19,28] These previous studies implicitly suggested that microstructural distribution features such as defect distribution, rather than strength distribution obtained from specific tests, are considered appropriate as common indicators for reliability design strategies for brittle components of the same lot.

Thus, in this study, we propose a novel strength evaluation scheme based on the new assumption that the distribution feature of the defect is constant, rather than the conventional assumption that the $m$-value, an indicator of strength distribution, is constant, as shown in Figure 1B. The proposed scheme can evaluate the strength scatter of components with diverse shapes and boundary conditions by using the inversely estimated defect distribution from standardized strength test results as a universal distribution indicator. This is difficult to achieve using the conventional scheme. Therefore, this will be a useful method for performing the reliability design of ceramic components

more efficiently and accurately. To demonstrate the scheme, the following topics are addressed in this study:

1. Particle swarm optimization (PSO),[32] a type of swarm intelligence optimization method, is applied to the forward analysis method (microstructural information → strength distribution)[15,21–23] to inversely estimate the defect distribution (equivalent crack length distribution) based on the results of standardized bending tests for alumina specimens.
2. The effectiveness of the proposed scheme for predicting the strength scatter of differently sized specimens under different loading conditions (other forward analyses) is discussed using the estimated equivalent crack length distribution.

The generalized extreme value (GEV) distribution,[33] a type of extreme value statistical model, is adopted for the mathematical description of significant equivalent cracks distribution because only large defects that could be fracture origins are the focus. Extreme value statistics have been widely applied in metal fatigue analysis, and the relationship between fatigue strength and inclusion size is discussed.[34–38] Studies have also been conducted on ceramics, relating pore size and cracks to static strength.[18,39–41]

## 2 | TARGET MATERIAL AND STANDARDIZED TESTS

In this study, AS999 (Ferrotec Material Technologies Corporation, Japan), sintered plates of high-purity alumina, were used as the target material. Reported dataset[15] for four types of bending tests with different effective volumes obtained by varying the external and internal span lengths were used to demonstrate the proposed scheme. The datasets include two types of three-point bending tests (3pb-S: external span length of 16 mm; 3pb-L: external span length of 30 mm) and two types of four-point bending tests (4pb-S: external span length of 30 mm; 4pb-L: external span length of 60 mm) with internal span lengths of 10 mm. Following the Japanese Industrial Standard (JIS R 1601), the surfaces of the specimens were mirror-polished, and the bending tests were conducted. The experimental setup comprised a bending testing machine (AG-X plus, 10 kN, Shimadzu Corporation) and attached bend test jigs. Here, bending tests were performed at a crosshead speed of 0.5 mm/s at room temperature. The specimens and test geometries are listed in Table 1. All the specimens used in the bending tests were fabricated from the same lot. Mode I fracture toughness $K_{IC}$ of AS999 was reported as 4.0 MPa $m^{0.5}$.[15]

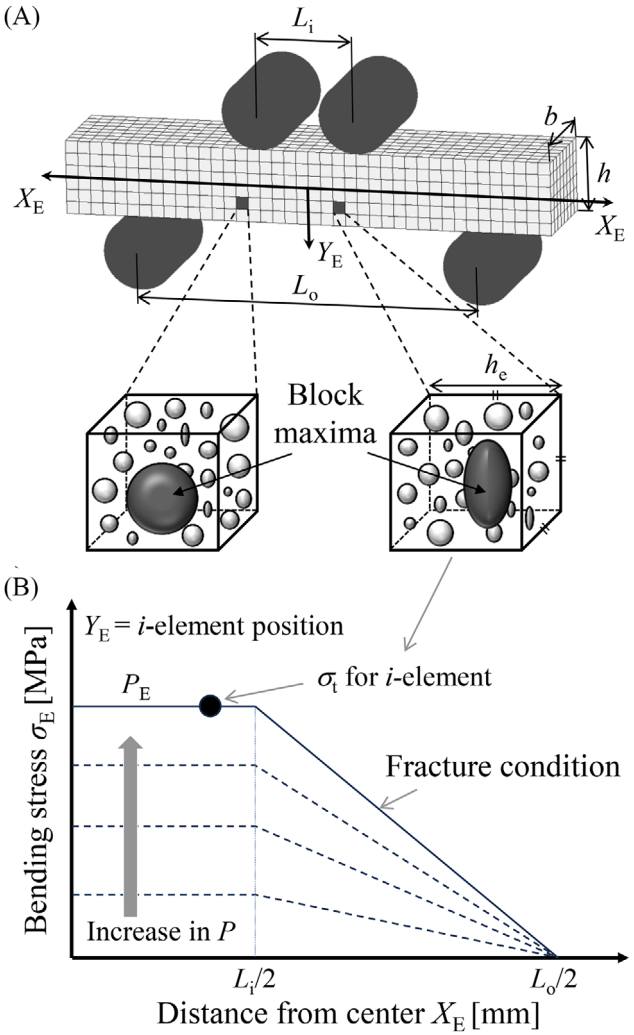


**FIGURE 2** Analysis model of bending test with the fracture mechanics model implemented: (A) specimen and test geometries, (B) schematic for determining the fracture load $P_E$ corresponding to the $i$-element of the specimen.

Bending strength $\sigma_B$ was obtained using Equation (1):

$$\sigma_B = \frac{3P_B(L_o - L_i)}{2bh^2}, \tag{1}$$

where $P_B$ is the peak value of the jig reaction force, $L_o$ is the external span length, $L_i$ is the internal span length, $b$ is the width of the specimen, and $h$ is the thickness of the specimen (Figure 2A).

The bending strength of each specimen was organized using the following two-parameter Weibull distribution (Equation 2)[42]:

$$F(\sigma_B) = 1 - \exp\left\{-\left(\frac{\sigma_B}{\beta}\right)^m\right\}, \tag{2}$$

where $m$ and $\beta$ are the Weibull modulus and scale parameter, respectively. Cumulative fracture probability $F(\sigma_B)$ was

**TABLE 1** Dimension of the test specimen, span length, and strength properties of the bending test.[15]

| | Specimen geometry | | Test geometry | | Strength property | | | |
|---|---|---|---|---|---|---|---|---|
| **Test type** | $b$ [mm] | $h$ [mm] | $L_o$ [mm] | $L_i$ [mm] | $m$ [–] | $\beta$ [MPa] | $\sigma_B^{0.007\%}$ | $\sigma_B^{99.99\%}$ |
| 3pb-S | 4 | 3 | 16 | 0 | 14.1 | 412.6 | 208.9 | 484.6 |
| 3pb-L | | | 30 | | 14.5 | 383.9 | 198.3 | 448.6 |
| 4pb-S | | | 30 | 10 | 14.9 | 352.1 | 185.0 | 409.8 |
| 4pb-L | | | 60 | | 18.9 | 338.3 | 203.8 | 381.3 |

*Note*: The Mode I fracture toughness $K_{IC}$ of AS999 was reported as 4.0 MPa $m^{0.5}$.[15]

calculated using the median rank method. Under each test condition, the number of specimens was $N = 30$.

The bending test results obtained under these conditions are listed in Table 1. Specifically, Weibull modulus $m$ and scale parameter $\beta$ determined using maximum likelihood estimation are listed. In addition, bending strengths for 0.007% and 99.99% cumulative fracture probability $\sigma_B^{0.007\%}$ and $\sigma_B^{99.99\%}$ corresponding to the weakest (ascending rank: 1) and strongest (ascending rank: 10 000) strength assuming $N = 10\,000$, respectively, are also shown. They were estimated from $m$ and $\beta$ in each test condition and Equation (2). The fracture origins of all test specimens were confirmed to be internal defects containing unsintered grains and not surface flaws caused by machining.[15]

## 3 | FORWARD ANALYSIS OF STRENGTH SCATTER

This section presents the forward analysis model for the bending tests. In addition, the application of extreme value statistics to describe equivalent cracks is explained.

### 3.1 | Analysis model of bending tests

To simulate the bending tests, the specimens were discretized with cubic elements on one side $h_e$, as shown in Figure 2A. When a load $P$ is applied, the bending stress occurring in each element $\sigma_E$ is given as Equation (3):

$$\sigma_E = \begin{cases} \frac{Y_E(L_o - L_i)}{4I} P & \text{for} \quad X_E < L_i/2 \\ \frac{Y_E(L_o/2 - X_E)}{2I} P & \text{for} \quad L_i/2 \le X_E < L_o/2 \end{cases}, \tag{3}$$

where $I$ is the moment of inertia of the area, $X_E$ is the distance from the center cross-section of the specimen to an arbitrary element (calculation point), and $Y_E$ is the distance from the neutral plane. In what follows, evaluation points of bending stresses $\sigma_E$ were selected at the center of each element.

Because the strength scatter in brittle ceramic components originates from differences in the location of fracture origins and differences in local strength owing to defect distribution, it is necessary to evaluate the local fracture stress. To evaluate the local fracture stress $\sigma_t$ around the intrinsic defects, we adopted the following Griffith/Irwin-type equation based on linear elastic fracture mechanics for the fracture mechanics model (Equation 4):

$$\sigma_t = \frac{K_{IC}}{\sqrt{\pi a_e}}, \tag{4}$$

where $a_e$ is the equivalent crack length corrected for shape effects for cracks of various shapes and lengths. As mentioned earlier, this study considered only internal defects because all specimens were fractured from defects containing unsintered grains.[15]

We explain the forward analysis, in which the scatter of the bending strength is numerically determined using the stress evaluation and fracture mechanics models given by Equations (3) and (4). First, the inverse function method[43] is applied to the appropriate cumulative distribution function of the equivalent crack length to generate random numbers for each element. Each equivalent crack length $a_e$ is then transformed into a local fracture stress $\sigma_t$ via the fracture mechanics model (Equation 4). This enables the generation of a specimen model with distributed local fracture stresses. Next, we evaluate the applied load $P$ when the bending stress $\sigma_E$ calculated using Equation (3) exceeds the local fracture stress $\sigma_t$ for each element, as shown in Figure 2B. The applied load when $\sigma_E$ exceeds $\sigma_t$ in each element is taken as $P_E$. The minimum $P_E$ within all elements is considered the peak load $P_B$ of the target specimen under test, and the bending strength $\sigma_B$ is calculated using Equation (1). By performing the same procedure for multiple specimen models, the strength scatter can be evaluated using a two-parameter Weibull distribution (Equation 2). The bending stress at the initial fracture and the bending strength (maximum bending stress) obtained from the bending test were assumed to be the same because the fine-grained alumina exhibits limited $R$-curve behavior.[44] In addition, the bending stress

distribution was assumed to be similar to that of fracture because the fine-grained alumina exhibits minimal plastic bulk deformation at room temperature.[45]

### 3.2 | Distribution function of equivalent crack length

Because the largest equivalent crack in an element (block maxima) can be a candidate for the fracture origin of each element, we focused only on the largest equivalent cracks in each element (see Figure 2A). Therefore, the GEV model was employed to statistically describe the distribution characteristics of a large equivalent crack length $a_e$. In the GEV model, all the data of interest are divided into blocks of equal size, and the maximum values of each block are treated. In the analysis, the blocks correspond to elements. The cumulative distribution function $G$ and probability density function $g$ of the GEV distribution are given by Equations (5) and (6)[33,46]:

$$G(a_e) = \begin{cases} \exp\left\{-\left[1+\xi\left(\frac{a_e-\mu}{\sigma}\right)\right]^{-1/\xi}\right\} & \text{for } \xi \neq 0 \\ \exp\left\{-\exp\left[-\left(\frac{a_e-\mu}{\sigma}\right)\right]\right\} & \text{for } \xi = 0 \end{cases}, \tag{5}$$

$$g(a_e) = \begin{cases} \exp\left\{-\left[1+\xi\left(\frac{a_e-\mu}{\sigma}\right)\right]^{-1/\xi}\right\}\frac{1}{\sigma}\left\{1+\xi\left(\frac{a_e-\mu}{\sigma}\right)\right\}^{-1/\xi-1} & \text{for } \xi \neq 0 \\ \exp\left\{-\exp\left[-\left(\frac{a_e-\mu}{\sigma}\right)\right]\right\}\frac{1}{\sigma}\exp\left(-\frac{a_e-\mu}{\sigma}\right) & \text{for } \xi = 0 \end{cases}, \tag{6}$$

where $\mu$, $\sigma$, and $\xi$ are the location, scale, and shape parameters, respectively. The shape parameter $\xi$ is closely related to the tail behavior of its probability density function. In particular, when the distribution is a long-tailed type with no maximum value, it is called the Fréchet distribution in the case of $\xi > 0$. By contrast, a short-tailed type with a finite upper endpoint is called a negative Weibull distribution. Moreover, it corresponds to the Gumbel distribution in the case of $\xi = 0$.[33,46]

## 4 | INVERSE ANALYSIS OF THE EQUIVALENT CRACK LENGTH DISTRIBUTION

This section describes a method for the inverse estimation of the equivalent crack length distribution corresponding to block maxima data using the standardized test results shown in Figure 1B. The objective function was set based on the Weibull plot indices obtained from the bending tests shown in Table 1, and the parameters of the GEV model that can reproduce the strength scatter were optimized. In this study, PSO[32] was employed among various optimization methods.

PSO is a heuristic optimization method based on the collective behavior of a flock of animals such as fish and birds. This method is widely used in various fields owing to the simplicity of the algorithm, smaller number of control parameters, and high convergence to a solution.[47–51] In the PSO, many particles (search individuals), which are candidate solutions, are placed in the solution space to search for an optimal solution. The migration paths of the particles in the dimensional space corresponding to parameters of the GEV model ($\mu$, $\sigma$, and $\xi$) are determined based on the experience and knowledge of each particle and the entire flock during the optimization process. The optimization process involves forward analysis using the current parameters of the GEV model possessed by each particle to evaluate the fitness of the experimental results. The details of the PSO algorithm (Figures S1 and S2), the response surface of the objective function (Figures S3 and S4), the effects of particle population (Figures S5 and S6), and the parameter settings (Table S1) are described in the Supporting Information Materials.

In PSO, the fitness level of each particle having ($\mu$, $\sigma$, $\xi$)-values is evaluated using an objective function. In this study, Equation (7) was adopted as the objective function (*Error*) to ensure that the properties of the Weibull plot obtained from the experiment and simulation are consistent.

$$Error = \sum_{i=1}^{n_{ref}} \left\{ \left( \frac{\ln \sigma_{Exp}^{0.007\%} - \ln \sigma_{Sim}^{0.007\%}}{\ln \sigma_{Exp}^{0.007\%}} \right)^2 + \left( \frac{\ln \sigma_{Exp}^{99.99\%} - \ln \sigma_{Sim}^{99.99\%}}{\ln \sigma_{Exp}^{99.99\%}} \right)^2 \right\}, \tag{7}$$

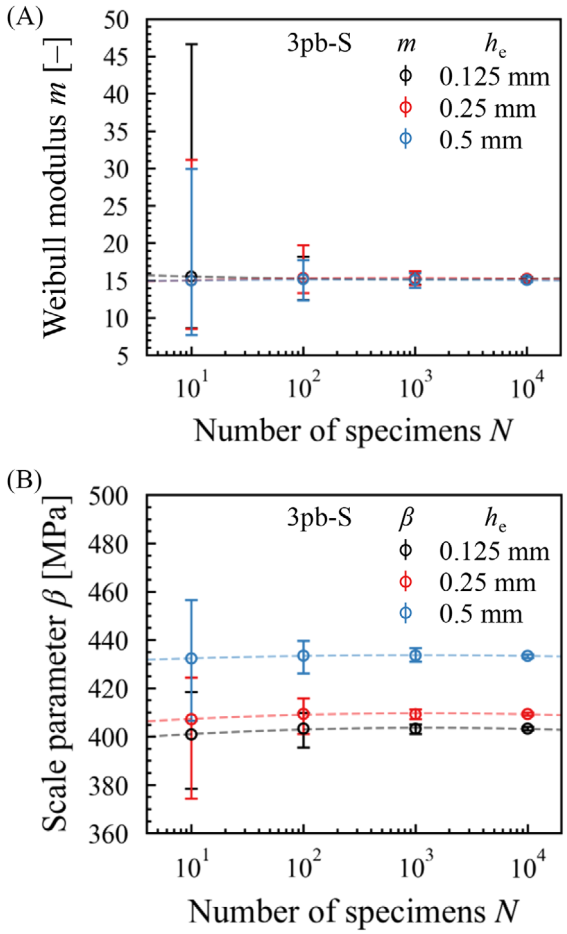


**FIGURE 3** Effect of number of specimens on scatter in (A) Weibull modulus $m$, (B) scale parameter $\beta$. Three different element sizes are used for the examination. The test condition in the simulation is the 3pb-S shown in Table 1. The input material properties and microstructural information are those reported by Ito et al.[15] Each plot and its error bar show the mean value and the minimum and maximum values, respectively, for 100 simulations.

where $\sigma^{0.007\%}$ and $\sigma^{99.99\%}$ are the strengths for 0.007% and 99.99% cumulative fracture probability, corresponding to the weakest and strongest strength in $N = 10\,000$ specimens, respectively. The subscripts "Exp" and "Sim" denote values obtained from experiment and simulation, respectively. As described in Section 2, $\sigma^{0.007\%}$ and $\sigma^{99.99\%}$ are calculated using the Weibull distribution parameters $m$ and $\beta$. Because the strengths of the higher and lower cumulative fracture probabilities strongly reflect the characteristics of the Weibull distribution parameters, we used the upper- and lower-limit strengths for the objective function. Here, the population of equivalent cracks that could be fracture origins was assumed to be the same in the range of stress levels from $\sigma^{0.007\%}$ to $\sigma^{99.99\%}$. $n_{ref}$ in Equation (7) is the number of reference test (experimental) types.

The Weibull distribution parameters obtained using insufficient specimens showed dispersion in both experiments and simulations. In these cases, the fitness level lacks stability and reliability. Therefore, the forward strength analysis in the optimization was conducted using a sufficient number of specimens, which ensured the stability of the Weibull distribution parameters in this study. Figure 3A,B shows the dispersion of the Weibull modulus $m$ and scale parameter $\beta$ depending on the number of specimens in the simulation, respectively, whose test type is 3pb-S in Table 1. Here, the fracture toughness $K_{IC} = 4.0$ MPa m$^{0.5}$ and microstructural information (internal defect distribution) of AS999 reported by Ito et al.[15] were input, and the discretized size per side of elements in the simulation was set to $h_e = 0.125$, 0.25, and 0.5 mm. The maximum, minimum, and mean values of the Weibull modulus and the scale parameter are shown by error bars, where 100 simulations were performed for each number of specimens. The Weibull modulus $m$ converged to almost the same value regardless of element size $h_e$, whereas the scale parameter $\beta$ tended to increase as the element size increased. This is due to the difference in stress evaluation points: as in the ordinary finite element method, the larger the element size, the smaller the evaluated bending stress value (Equation 3). However, independent of element size, both the Weibull modulus and the scale parameter became more stable as the number of specimens increased. Therefore, $N = 10\,000$ specimens were used for forward analysis in the PSO optimization because of the stability of the Weibull distribution parameters and computational cost.

## 5 | RESULTS AND DISCUSSION

### 5.1 | Estimation of equivalent crack length distribution and reproducibility of strength scatter

First, the GEV distribution of equivalent crack lengths when the block size is one element under the element size $h_e = 0.25$ mm was estimated based on the results of the 3pb-S strength test ($n_{ref} = 1$). The search ranges for the GEV model parameters were $\mu = 0$–30 μm, $\sigma = 0$–10 μm, and $\xi = -0.5$–0.5. The fracture toughness $K_{IC}$ in Equation (4), required for the PSO optimization analysis, was set to 4.0 MPa m$^{0.5}$.[15]

Figure 4A,B shows the inversely estimated equivalent crack length distributions and measured equivalent crack length data based on microstructural observations using the probability density and Gumbel probability paper, respectively. Here, the estimation of the equivalent crack length distribution was performed five times. The

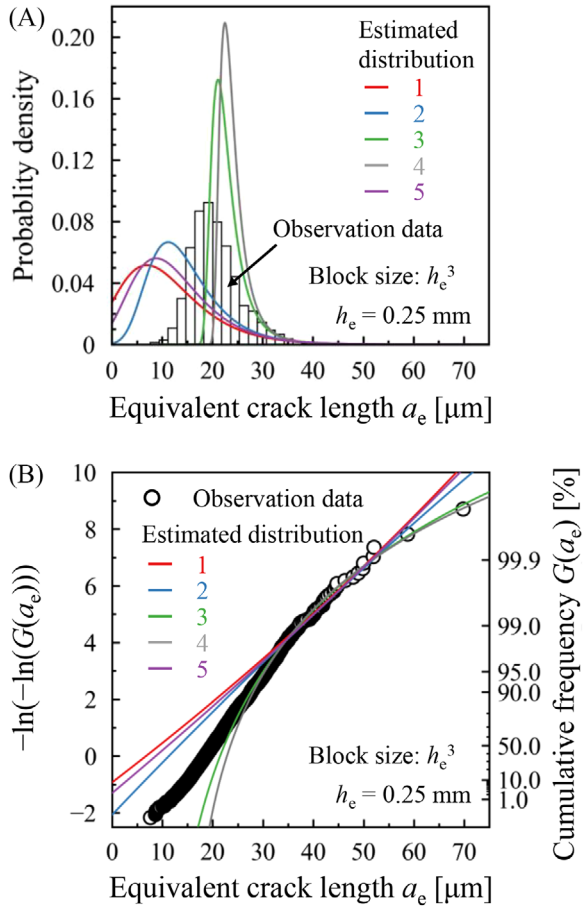


**FIGURE 4** Estimated equivalent crack length distributions based on experimental strength data under 3pb-S, and 4224 datapoints of equivalent crack length converted from the results of microstructural observation[15]: (A) probability density; (B) Gumbel probability paper.

**TABLE 2** Parameters of the estimated equivalent crack length distributions shown in Figure 4.

| Label | Location $\mu$ [μm] | Scale $\sigma$ [μm] | Shape $\xi$ [–] |
|---|---|---|---|
| Sim. 1 | 6.8 | 7.1 | −0.03 |
| Sim. 2 | 11.3 | 5.5 | 0.02 |
| Sim. 3 | 21.5 | 2.2 | 0.18 |
| Sim. 4 | 22.8 | 1.8 | 0.22 |
| Sim. 5 | 8.7 | 6.6 | −0.02 |

observation-based data in the figures were converted to equivalent crack lengths by referring to the distributions of pore size (major pore radius), pore aspect ratio (minor pore radius/major pore radius), and grain size for the same lot of AS999 reported by Ito et al.[15] In addition, the block maxima data of equivalent crack lengths for 4224 elements of the same size as those in the optimization analysis were generated for comparison. Table 2 lists the estimated equivalent crack length distribution parameters ($\mu$, $\sigma$, and

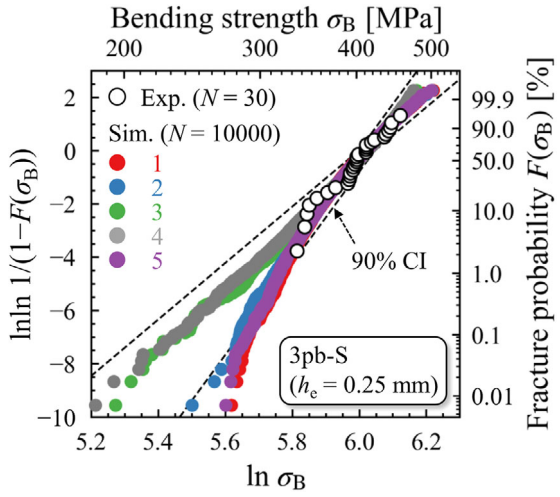


**FIGURE 5** Comparison of Weibull plots between experimental and simulation results for $N$ = 10 000 specimens under 3pb-S using estimated equivalent crack length distributions shown in Figure 4. Dashed lines represent the 90% confidence interval of experimental results based on the maximum likelihood estimation of the Weibull distribution.

$\xi$). The estimated parameters showed large variations for the performed numbers (five times) and did not perfectly agree with the observed distribution. In particular, both positive and negative values were estimated for the shape parameter $\xi$, resulting in large differences in the tail behaviors of the distribution, as shown in Figure 4B. Nevertheless, the distribution properties are broadly consistent for cumulative probabilities within the limited range from approximately 90% to 99.9% (see Figure 4B).

Figure 5 shows a comparison of the Weibull plots of the bending strengths for the 3pb-S test obtained from the experiment ($N$ = 30) and forward analysis ($N$ = 10 000), which uses the inversely estimated equivalent crack length distributions shown in Figure 4. Here, the element size in the forward analysis was the same as in the optimization analysis: $h_e$ = 0.25 mm. The dashed lines correspond to the 90% confidence intervals of the experimental results. As seen from Figure 5, the results of all the forward analyses using the estimated distributions agree well with the experimental result, within the range of cumulative fracture probabilities ranging from approximately 10% to 90%. By contrast, the lower strength properties strongly reflect the characteristics of the input equivalent crack length distributions. For distributions with a positive shape parameter $\xi$, that is, no maximum equivalent crack length, the Weibull plot becomes a straight-line distribution (Sim. 3 and Sim. 4). For distributions with a negative shape parameter $\xi$, the Weibull plot becomes a curve-type with a lower limit of strength (Sim. 1 and Sim. 5). Table 3 lists the Weibull distribution parameters of the forward analysis results shown in Figure 5. The Weibull

**TABLE 3** Weibull distribution parameters of the results of the forward analyses shown in Figure 5.

| Label | $m$ [–] | $\beta$ [MPa] |
|---|---|---|
| Sim. 1 | 14.0 | 413.1 |
| Sim. 2 | 14.2 | 413.0 |
| Sim. 3 | 14.2 | 412.2 |
| Sim. 4 | 14.0 | 412.3 |
| Sim. 5 | 14.1 | 413.0 |

distribution parameters have almost identical values, although the lower strength properties differ widely. This means that the Weibull distribution parameters are largely influenced by the strength data with a cumulative fracture probability of approximately 10% to 90%. In the case of test condition 3pb-S, the equivalent crack lengths to reproduce the experimental strengths with cumulative fracture probabilities from approximately 10% to 90% correspond to approximately 90% to 99.9% of the cumulative probabilities in Figure 4B, and hence the distribution properties are consistent in this region ($N = 30$).

## 5.2 | Effect of reference test data on inverse estimation

A key to the reliable design of components is the accurate estimation of the defect distribution over a wide size range because the size of the defects that can become fracture origins depends on the size and shape of the component and the boundary condition. In Section 5.1, it was confirmed that the estimated equivalent crack length distributions agree with the microstructural observation data only in the range of equivalent crack lengths corresponding to the candidate of fracture origins in the reference test (strength test results used for the inverse analysis). Therefore, in this section, the experimental results of strength tests for 3pb-S and 4pb-S listed in Table 1 were simultaneously used as reference tests for a single estimation of equivalent crack length distribution ($n_{\mathrm{ref}} = 2$). This is expected to allow a wider range of equivalent crack lengths as candidates for fracture origins to be estimated.

3pb-S was selected as one of the reference tests because it has the smallest effective volume, that is, the small equivalent crack could be a candidate fracture origin, among the four test conditions listed in Table 1. 4pb-S was selected because it is a test condition of JIS and has a large effective volume. Here, the element size was set to $h_{\mathrm{e}} = 0.25$ mm, as in Section 5.1. The search ranges of the GEV model parameters were set to $\mu$ = 0–30 μm, $\sigma$ = 0–10 μm, and $\xi = -0.5$–0.5.

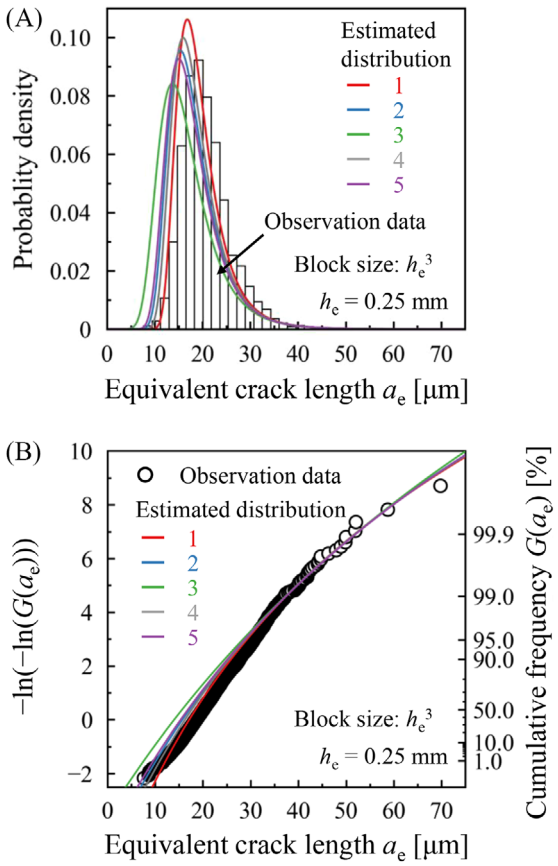


**FIGURE 6** Estimated equivalent crack length distributions based on experimental strength data under 3pb-S and 4pb-S, and 4224 datapoints of equivalent crack length converted from the results of microstructural observation[15]: (A) probability density; (B) Gumbel probability paper.

**TABLE 4** Parameters of the estimated equivalent crack length distributions shown in Figure 6.

| Label | Location $\mu$ [μm] | Scale $\sigma$ [μm] | Shape $\xi$ [–] |
|---|---|---|---|
| Sim. 1 | 17.1 | 3.5 | 0.10 |
| Sim. 2 | 15.7 | 3.9 | 0.08 |
| Sim. 3 | 14.0 | 4.4 | 0.06 |
| Sim. 4 | 16.3 | 3.7 | 0.09 |
| Sim. 5 | 15.3 | 4.0 | 0.08 |

Figure 6 shows a comparison of inversely estimated equivalent crack length distributions and measured equivalent crack length data obtained from microstructural observations. Figure 6A,B shows the probability density and Gumbel probability paper, respectively. Estimation of the equivalent crack length distribution was performed five times. Table 4 lists the estimated equivalent crack length distribution parameters ($\mu$, $\sigma$, and $\xi$). Compared with the results obtained using only 3pb-S as the reference test (see Section 5.1), the estimated equivalent crack length distribution showed less scatter and better agreement with

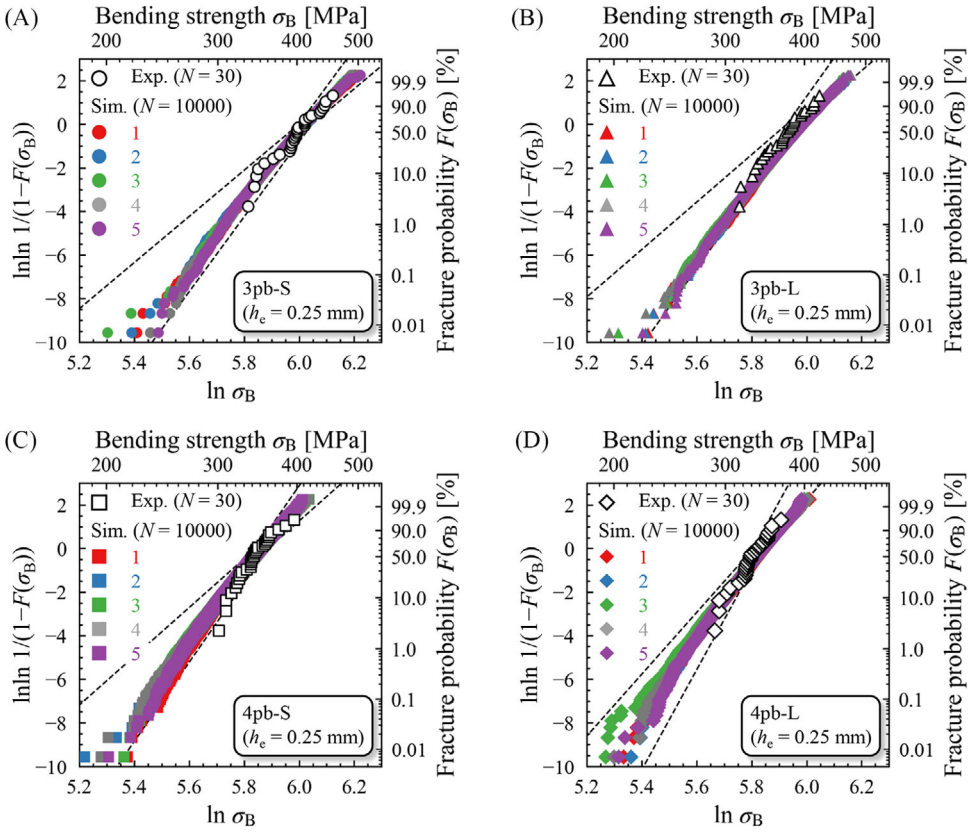


**FIGURE 7** Comparison of Weibull plots between experimental and simulation results for $N = 10\,000$ specimens under (A) 3pb-S; (B) 3pb-L; (C) 4pb-S; and (D) 4pb-L using estimated equivalent crack length distributions shown in Figure 6. Dashed lines represent the 90% confidence interval of experimental results based on the maximum likelihood estimation of the Weibull distribution.

the observation-based data. These results indicate that it is more effective to use strength test results under multiple conditions as reference tests, particularly a combination of those such that the fracture origin size is widely distributed. Hence, to inversely estimate equivalent crack length distribution more efficiently from a test cost standpoint, it is effective to use reference test conditions with as small and as large effective volumes as possible. As a result, the uniqueness of the inversely estimated distributions and the agreement with the true value of the distribution would be guaranteed not only on the tail side but also on the smaller side.

The accuracy of the strength data of the reference tests also significantly affects the accuracy of the inversely estimated equivalent crack length distribution. The reliability of the Weibull distribution parameters is highly affected by the number of specimens, particularly when the number of specimens is small,[14,20] as shown in Figure 3. Therefore, to improve the accuracy of the estimated equivalent crack length distributions, it is ideal to increase the number of specimens in the standardized test to obtain highly reliable strength data.

Figure 7 shows comparisons of the Weibull plots of the bending strengths for the 3pb-S, 3pb-L, 4pb-S, and 4pb-L tests obtained from the experiments ($N$ = 30) and forward analyses ($N$ = 10 000), which use the inversely estimated equivalent crack length distributions shown in Figure 6. Here, the element size in the forward analyses was the same as in the optimization analysis: $h_e$ = 0.25 mm. The dashed lines correspond to the 90% confidence intervals of the experimental results. The results of the forward analyses reasonably predicted not only the strength scatter of 3pb-S and 4pb-S, which were the target of optimization but also the scatter under different test conditions (3pb-L and 4pb-L) with different sizes and loading conditions. It is suggested that the proposed strength evaluation scheme which inversely estimates the equivalent crack length distribution of the target lot from the standardized strength test and evaluates the strength scatter of components with diverse shapes and boundary conditions using it as an input parameter, is effective.

The proposed scheme allows the direct evaluation of the strength scatter of the target components using FEA[15,21–23] without the need to analyze the size dependency on the strengths of the ceramic components or to evaluate the effective volume in advance. In addition, the lower strength limit for a large number of components can be

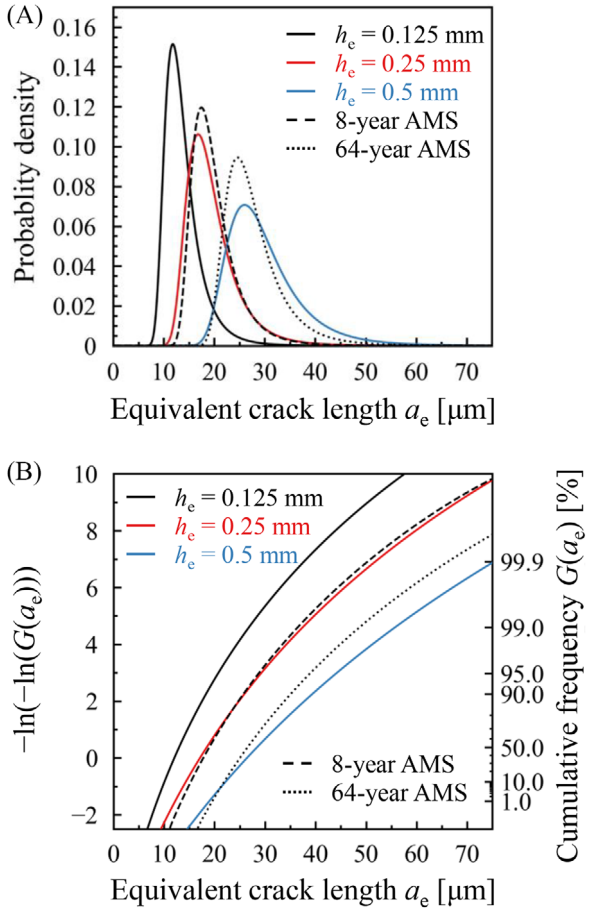


**FIGURE 8** Estimated equivalent crack length distributions based on experimental strength data under 3pb-S and 4pb-S with $h_e$ = 0.125, 0.25, and 0.5 mm, and equivalent crack length distributions of 8- and 64-year AMS obtained from the distribution estimated with $h_e$ = 0.125 mm: (A) probability density; (B) Gumbel probability paper.

evaluated by performing a forward analysis using the estimated equivalent crack length distribution, as shown in Figure 7.

## 5.3 | Impact of model discretization

The effect of element discretization in the proposed scheme is discussed. Because the GEV model employed in this study was based on the "block maxima concept", the correspondence between the element sizes of the optimization and forward analyses should be noted.

Figure 8A,B shows the inversely estimated equivalent crack length distributions in the probability density and the Gumbel probability paper, respectively, where the element size was set to $h_e$ = 0.125, 0.25, and 0.5 mm. The optimization targets were the 3pb-S and 4pb-S test results, and the search ranges for the GEV model parameters were $\mu$ = 0–30 μm, $\sigma$ = 0–10 μm, and $\xi$ = −0.5–0.5. The estimated equivalent crack length distribution with $h_e$ = 0.25 mm corresponds to the result of Sim. 1 in Figure 6. The figures also show the equivalent crack length distributions of 8- and 64-year annual maximum series (AMS) with 8- and 64-times block sizes ($0.25^3$ mm$^3$ and $0.5^3$ mm$^3$) obtained from the distribution estimated with $h_e$ = 0.125 mm. Here, the distribution function $G_n(x)$ of the $n$-year AMS can be expressed using that of reference (1-year) AMS $G(x)$ by the "statistics of extremes" as Equation (8)[52]:

$$G_n(x) = [G(x)]^n. \tag{8}$$

Figure 8 confirms the estimated distribution shifts to the larger side for larger element size $h_e$. This reflects the fact that, as the block size (element volume) increases, larger equivalent cracks can exist within that volume. Comparing the distributions of $n$-year AMS obtained from the estimated distribution with $h_e$ = 0.125 mm (hereafter referred to as $n$-year AMS) with the directly estimated distribution with respective element sizes, the distribution of the 8-year AMS and the directly estimated distribution is almost identical for $h_e$ = 0.25 mm. In contrast, for $h_e$ = 0.5 mm, the distribution of the 64-year AMS is slightly smaller than the directly estimated distribution, particularly in the tail region. This is due to the accuracy of the calculated bending stress distribution (Equation 3). In general, the finer the discretization, the more accurately the stress distribution is evaluated in the bending test analysis as described in Section 4. Therefore, even if equal local fracture stresses are distributed to the bottom elements between the inner spans in a four-point bending test analysis, where the calculation points are at the center of respective elements, the bulk strength of the specimens with larger element sizes will be higher. In this scheme, the estimated equivalent crack length distribution with $h_e$ = 0.5 mm was intended to reproduce the experimental strength scatter using the element size used in the optimization rather than the actual equivalent crack length distribution. Thus, the optimized distribution with $h_e$ = 0.5 mm was slightly larger than the 64-year AMS, whereas the strength distribution characteristics were consistent with the experimental results.

Figure 9A–C shows the results of the forward analysis of the bending tests for $N$ = 10 000 specimens using the inversely estimated equivalent crack length distribution with $h_e$ = 0.125 mm and the equivalent crack length distributions of 8- and 64-year AMS shown in Figure 8, respectively. Here, the element size in the forward analysis is 0.125 mm, 0.25 mm (8-year AMS), and 0.5 mm (64-year AMS), respectively. The figures also show the experimental results listed in Table 1. As shown in Figure 8, the equivalent crack length distribution differs depending on the

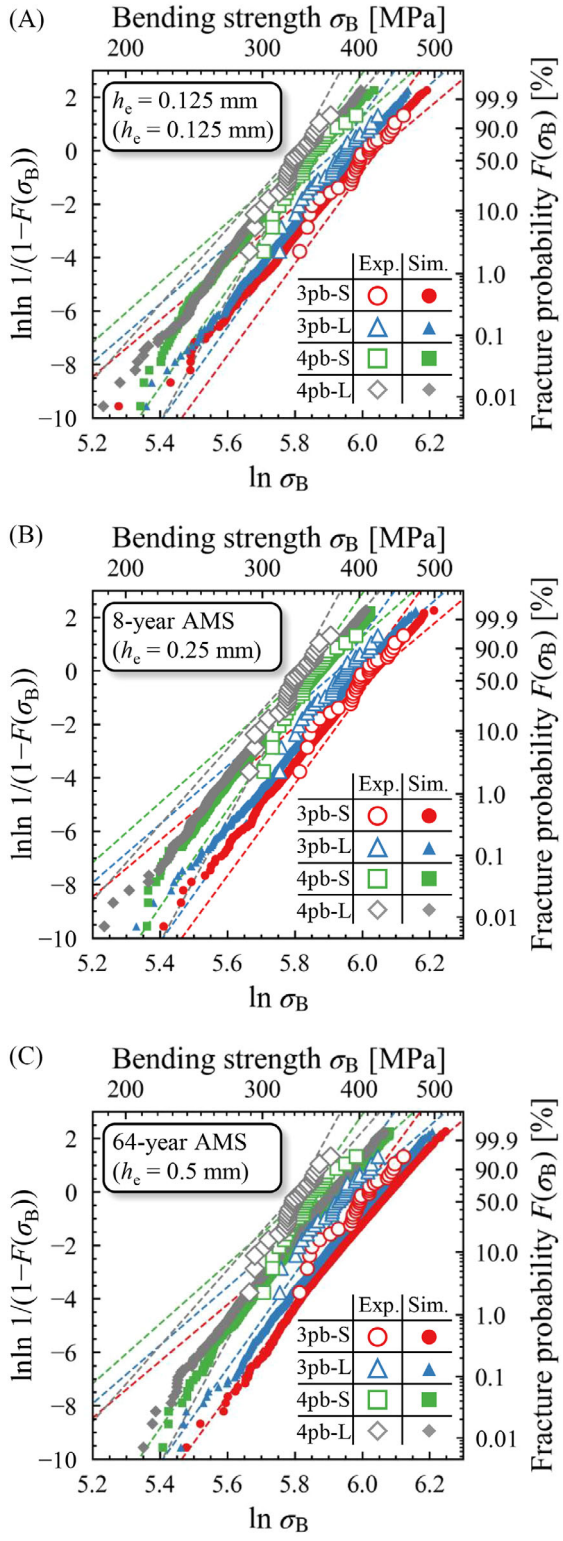


**FIGURE 9** Comparison of Weibull plots between experimental and simulation results using (A) estimated equivalent crack length distribution with $h_e = 0.125$ mm, (B) equivalent crack length distribution of 8-year AMS, and (C) equivalent crack length distribution of 64-year AMS shown in Figure 8. The element size in the forward analysis is $h_e = 0.125$, 0.25, and 0.5 mm, respectively. Dashed lines represent the 90% confidence interval of the experimental results.

element size in the optimization; however, the results of the forward analyses in Figure 9A reproduce the strength distribution in the experiment well for all test conditions. The same tendency is confirmed for the results of the forward analyses in Figure 9B using the equivalent crack length distribution of 8-year AMS. However, the results of the forward analyses in Figure 9C using the equivalent crack length distribution of 64-year AMS tend to be higher than the experimental results, reflecting the results shown in Figure 8. It is believed that 64-year AMS can also be used for forward analysis with $h_e = 0.5$ mm, provided that the stress distribution is limited (e.g., low-stress gradient and simple tensile cases). Ito et al.[15] reported that the results of the forward analyses for the same test conditions with $h_e = 0.125$, 0.25, and 0.5 mm showed that the strength scatter with $h_e = 0.125$ and 0.25 mm were almost identical.

The impact of model discretization in the proposed scheme can be summarized as follows:

1. To inversely estimate the equivalent crack length distribution, adopting an element size that can accurately reproduce the stress distribution (e.g., the bending stress distribution) in the standardized test is desirable. Then, the estimation results ($h_e \leq 0.25$ mm in this case) are generally consistent with the actual equivalent crack length distribution characteristics of the target material, as shown in Figure 6.
2. When the equivalent crack length distribution obtained in item 1 is applied as input parameters to a boundary value problem with arbitrarily shaped components and under arbitrary loading conditions, $n$-year AMS can be used to handle discretization arbitrarily $n$ times larger than the element size used in the optimization, provided that the stress distribution in the model is appropriate.

## 6 | OUTLOOK

In this study, only internal defects were considered because all specimens used the reference tests that fractured from them. However, it is difficult to eliminate surface flaws in actual components by machining due to productivity aspects, particularly in large components, resulting in a mixture of internal and surface defects as fracture origins.[53–55] The proposed scheme assumes that the defects causing fracture can be organized in the same population. Therefore, it is important to conduct screening based on fracture surface observations on the specimens used in the standardized tests and classify them into types of fracture origins (e.g., internal or surface, pores or inclusions). In the case of standardized tests in which the fracture origins are both internal and surface defects, it can be handled

by conducting inverse estimation of the defect distribution separately for each, and inputting the inversely estimated internal and surface defect distributions for each internal and surface element when predicting the strength scatter of the actual components. Here, it should be noted that the definition of the unit block from which the maximum value is extracted may be different when organizing internal and surface defects using the GEV model. In the case of internal defects, it is the largest per volume, whereas in the case of surface defects, it is the largest per area. To make the proposed scheme more versatile, we should verify this point in the future.

Meanwhile, it is also important to estimate "the allowable surface crack size", which is the surface crack size that does not affect the strength performance of the component, and to eliminate in advance any component with surface cracks larger than the allowable surface crack size. Using the proposed scheme, one predicts the strength scatter of components with diverse shapes and boundary conditions based on the results of a standardized strength test. Hence, by subsequently comparing the relationship between the strength scatter due to internal defects and the fracture strength due to surface crack, it could also be possible to evaluate the allowable surface crack size.[56]

## 7 | CONCLUSION

In this study, we proposed a strength evaluation scheme for the reliability design of brittle ceramic components. The effectiveness of the proposed scheme was demonstrated by comparing the results of the microstructural observations with the equivalent crack length distribution obtained by PSO estimation. It was also confirmed that the inversely estimated equivalent crack length distribution could be used to predict the strength scatter for the specimens of the four types of bending tests with different sizes and under loading conditions. The versatility and caveats of the scheme were discussed by examining the selection of the standardized strength (reference) tests and the impact of model discretization on the estimation of the equivalent crack length distribution. Even for brittle ceramic components that exhibit scatter and size dependency of strength, it is possible to predict the strength scatter under different boundary conditions using microstructural properties, such as equivalent crack length distribution, as a common indicator. In this study, the GEV distribution was employed as the probability density function describing the defect distribution of ceramics. Still, other distributions such as log-normal and power-law types can be used. Furthermore, the optimization method can be substituted for algorithms such as genetic and reinforcement learning algorithms.

However, because the inverse estimation performance of defect distribution depends on the objective function, a review of the objective functions will be considered in future research. In addition, the proposed scheme assumes a single population of large defects inside the components. However, they may differ between the near-surface and interior regions in cases of large components and additive manufacturing materials. The effect of such differences in microstructural properties on strength properties should be considered. Moreover, in this study, although the validity of the proposed scheme was verified for only one type of alumina, the applicability to other ceramics such as silicon nitride[57–60] should be examined in the future. Here, we believe that the proposed scheme can be applied to other brittle materials, particularly when the forward analysis can predict the results of the standardized tests of the target materials. We will address these issues to generalize the proposed scheme in the future.

## ACKNOWLEDGMENTS

This article is based on results obtained from a project, JPNP22005, commissioned by the New Energy and Industrial Technology Development Organization (NEDO).

## ORCID

*Taiyo Maeda* https://orcid.org/0009-0007-4552-7251
*Toshio Osada* https://orcid.org/0000-0003-1539-9264
*Shingo Ozaki* https://orcid.org/0000-0003-3450-6774

## REFERENCES

1. Ohnabe H, Masaki S, Onozuka M, Miyahara K, Sasa T. Potential application of ceramic matrix composites to aero-engine components. Compos A. 1999;30(4):489–96. https://doi.org/10.1016/S1359-835X(98)00139-0
2. Lu ZL, Fan YX, Miao K, Jing H, Li DC. Effects of adding aluminum oxide or zirconium oxide fibers on ceramic molds for casting hollow turbine blades. Int J Adv Manuf Technol. 2014;72(5–8):873–80. https://doi.org/10.1007/s00170-014-5723-9
3. Vaferi K, Vajdi M, Nekahi S, Nekahi S, Sadegh Moghanlou F, Shahedi Asl M, et al. Thermo-mechanical simulation of ultrahigh temperature ceramic composites as alternative materials for gas turbine stator blades. Ceram Int. 2021;47(1):567–80. https://doi.org/10.1016/j.ceramint.2020.08.164
4. Dhanasekar S, Ganesan AT, Rani TL, Vinjamuri VK, Nageswara Rao M, Shankar E, et al. A comprehensive study of ceramic matrix composites for space applications. Adv Mater Sci Eng. 2022;2022(1):1–9. https://doi.org/10.1155/2022/6160591
5. Karadimas G, Salonitis K. Ceramic matrix composites for aero engine applications—A review. Appl Sci. 2023;13(5):3017. https://doi.org/10.3390/app13053017
6. Deckers J, Vleugels J, Kruth J-P. Additive manufacturing of ceramics: a review. J Ceram Sci Technol. 2014;5(4):245–60.
7. Zocca A, Colombo P, Gomes CM, Günster J. Additive manufacturing of ceramics: issues, potentialities, and opportunities.

J Am Ceram Soc. 2015;98(7):1983–2001. https://doi.org/10.1111/jace.13700
8. Lakhdar Y, Tuck C, Binner J, Terry A, Goodridge R. Additive manufacturing of advanced ceramic materials. Prog Mater Sci. 2021;116:100736. https://doi.org/10.1016/j.pmatsci.2020.100736
9. Pelz JS, Ku N, Meyers MA, Vargas-Gonzalez LR. Additive manufacturing of structural ceramics: a historical perspective. J Mater Res Technol. 2021;15:670–95. https://doi.org/10.1016/j.jmrt.2021.07.155
10. Dadkhah M, Tulliani JM, Saboori A, Iuliano L. Additive manufacturing of ceramics: advances, challenges, and outlook. J Eur Ceram Soc. 2023;43(15):6635–64. https://doi.org/10.1016/j.jeurceramsoc.2023.07.033
11. Kaikai X, Yadong G, Qiang Z. Comparison of traditional processing and additive manufacturing technologies in various performance aspects: a review. Arch Civ Mech Eng. 2023;23(3):188. https://doi.org/10.1007/s43452-023-00699-3
12. Quinn GD, Morrell R. Design data for engineering ceramics: a review of the flexure test. J Am Ceram Soc. 1991;74(9):2037–66.
13. Bažant ZP. Size effect on structural strength: a review. Arch Appl Mech. 1999;69:703–25.
14. Danzer R, Lube T, Supancic P, Damani R. Fracture of ceramics. Adv Eng Mater. 2008;10(4):275–98.
15. Ito C, Maeda T, Higashi R, Osada T, Kohata T, Ozaki S. Application of extreme value statistics to internal pore distribution in ceramics and prediction of size dependency of strength scatter. J Eur Ceram Soc. 2024;44(5):3381–92.
16. Batdorf SB, Crose JG. A statistical theory for the fracture of brittle structures subjected to nonuniform polyaxial stresses. J Appl Mech. 1974;41(2):459–64.
17. Evans AG, Jones RL. Evaluation of a fundamental approach for the statistical analysis of fracture. J Am Ceram Soc. 1978;61(3–4):156–60.
18. Andreasen JH. Reliability-based design of ceramics. Mater Des. 1994;15(1):3–13.
19. Cook RF, DelRio FW. Determination of ceramic flaw populations from component strengths. J Am Ceram Soc. 2018;102(8):4794–808. https://doi.org/10.1111/jace.16262
20. American Society for Testing and Materials. Standard practice for reporting uniaxial strength data and estimating Weibull distribution parameters for advanced ceramics 2009;C1239–07. Annual Book of ASTM Standards:15.
21. Ozaki S, Aoki Y, Osada T, Takeo K, Nakao W. Finite element analysis of fracture statistics of ceramics: effects of grain size and pore size distributions. J Am Ceram Soc. 2018;101(7):3191–204.
22. Takeo K, Aoki Y, Osada T, Nakao W, Ozaki S. Finite element analysis of the size effect on ceramic strength. Materials (Basel). 2019;12(18):2885. https://doi.org/10.3390/ma12182885
23. Ozaki S, Yamagata K, Ito C, Kohata T, Osada T. Finite element analysis of fracture behavior in ceramics: prediction of strength distribution using microstructural features. J Am Ceram Soc. 2022;105(3):2182–95.
24. Evans AG. Structural reliability: a processing-dependent phenomenon. J Am Ceram Soc. 1982;65(3):127–37.
25. Seidel J, Claussen N, Rödel J. Reliability of alumina ceramics: effect of grain size. J Eur Ceram Soc. 1995;15(5):395–404.
26. Peterlik H. Relationship of strength and defects of ceramic materials and their treatment by Weibull theory. J Ceram Soc Jpn. 2001;109(8):S121–26.
27. Trunec M. Effect of grain size on mechanical properties of 3Y-TZP ceramics. Ceram Silik. 2008;52(3):165–71.
28. Cook RF, DelRio FW. Material flaw populations and component strength distributions in the context of the Weibull function. Exp Mech. 2019;59(3):279–93. https://doi.org/10.1007/s11340-018-0423-2
29. Okuma G, Watanabe S, Shinobe K, Nishiyama N, Takeuchi A, Uesugi K, et al. 3D multiscale-imaging of processing-induced defects formed during sintering of hierarchical powder packings. Sci Rep. 2019;9(1):11595. https://doi.org/10.1038/s41598-019-48127-y
30. Hu F, Zhu T, Xie Z, Liu J, Hu Z, An D. Elimination of grain boundaries and its effect on the properties of silicon nitride ceramics. Ceram Int. 2020;46(8):12606–12.
31. Wang A, Hu P, Zhao X, Wang Z, Zhang C, Wang Y. Modelling and experimental investigation of pore-like flaw-strength response in structural ceramics. Ceram Int. 2020;46(10):14431–38.
32. Eberhart R, Kennedy J. Particle swarm optimization. In: Proceedings of the IEEE international conference on neural networks; 1995:1942–48.
33. Kotz S, Nadarajah S. Extreme value distributions: theory and applications. London: Imperial College Press and Distributed by World Scientific Publishing Co. https://doi.org/10.1142/p191; 2000.
34. Beretta S, Anderson C, Murakami Y. Extreme value models for the assessment of steels containing multiple types of inclusion. Acta Mater. 2006;54(8):2277–89. https://doi.org/10.1016/j.actamat.2006.01.016
35. Wormsen A, Sjödin B, Härkegård G, Fjeldstad A. Non-local stress approach for fatigue assessment based on weakest-link theory and statistics of extremes. Fatigue Fract Eng Mat Struct. 2007;30(12):1214–27. https://doi.org/10.1111/j.1460-2695.2007.01190.x
36. Fjeldstad A, Wormsen A, Härkegård G. Simulation of fatigue crack growth in components with random defects. Eng Fract Mech. 2008;75(5):1184–203. https://doi.org/10.1016/j.engfracmech.2007.04.006
37. Wormsen A, Fjeldstad A, Härkegård G. A post-processor for fatigue crack growth analysis based on a finite element stress field. Comput Methods Appl Mech Eng. 2008;197(6–8):834–45. https://doi.org/10.1016/j.cma.2007.09.012
38. Beretta S. More than 25 years of extreme value statistics for defects: fundamentals, historical developments, recent applications. Int J Fatigue. 2021;151:106407. https://doi.org/10.1016/j.ijfatigue.2021.106407
39. Chao L-Y, Shetty DK. Extreme-value statistics analysis of fracture strengths of a sintered silicon nitride failing from pores. J Am Ceram Soc. 1992;75(8):2116–24. https://doi.org/10.1111/j.1151-2916.1992.tb04473.x
40. Bažant ZP, Pang SD. Activation energy based extreme value statistics and size effect in brittle and quasibrittle fracture. J Mech Phys Solids. 2007;55(1):91–131. https://doi.org/10.1016/j.jmps.2006.05.007

41. Nohut S. Influence of sample size on strength distribution of advanced ceramics. Ceram Int. 2014;40(3):4285–95. https://doi.org/10.1016/j.ceramint.2013.08.093
42. Weibull W. A statistical distribution function of wide applicability. J Appl Mech. 1951;18(3):293–97. https://doi.org/10.1115/1.4010337
43. Devroye L. Nonuniform random variate generation. In: Simulation. Amsterdam: Elsevier 2006:83–121. https://doi.org/10.1016/S0927-0507(06)13004-2
44. Tomaszewski H, Boniecki M, Weglarz H. Effect of grain size on R-curve behaviour of alumina ceramics. J Eur Ceram Soc. 2000;20(14–15):2569–74. https://doi.org/10.1016/S0955-2219(00)00137-0
45. Spriggs RM, Mitchell JB, Vasilos T. Mechanical properties of pure, dense aluminum oxide as a function of temperature and grain size. J Am Ceram Soc. 1964;47(7):323–27. https://doi.org/10.1111/j.1151-2916.1964.tb12994.x
46. Coles S. An introduction to statistical modeling of extreme values. London: Springer. https://doi.org/10.1007/978-1-4471-3675-0; 2001.
47. Zhu H, Wang Y, Wang K, Chen Y. Particle swarm optimization (PSO) for the constrained portfolio optimization problem. Expert Syst Appl. 2011;38(8):10161–69. https://doi.org/10.1016/j.eswa.2011.02.075
48. Jordehi AR. Particle swarm optimisation (PSO) for allocation of FACTS devices in electric transmission systems: a review. Renew Sustain Energy Rev. 2015;52:1260–67. https://doi.org/10.1016/j.rser.2015.08.007
49. Mousakazemi SMH, Ayoobian N. Robust tuned PID controller with PSO based on two-point kinetic model and adaptive disturbance rejection for a PWR-type reactor. Prog Nucl Energy. 2019;111:183–94. https://doi.org/10.1016/j.pnucene.2018.11.003
50. Pradhan A, Bisoy SK. A novel load balancing technique for cloud computing platform based on PSO. J King Saud Univ Comput Inf Sci. 2022;34(7):3988–95. https://doi.org/10.1016/j.jksuci.2020.10.016
51. Xing Z, Zhu J, Zhang Z, Qin Y, Jia L. Energy consumption optimization of tramway operation based on improved PSO algorithm. Energy. 2022;258:124848. https://doi.org/10.1016/j.energy.2022.124848
52. Gumbel EJ. Statistics of extremes. New York: Columbia University Press. https://doi.org/10.7312/gumb92958; 1958.
53. Quinn GD, Hoffman K, Quinn JB. Strength and fracture origins of a feldspathic porcelain. Dent Mater. 2012;28(5):502–11. https://doi.org/10.1016/j.dental.2011.12.005
54. Harrer W, Schwentenwein M, Lube T, Danzer R. Fractography of zirconia-specimens made using additive manufacturing (LCM) technology. J Eur Ceram Soc. 2017;37(14):4331–38. https://doi.org/10.1016/j.jeurceramsoc.2017.03.018
55. Scherrer SS, Lohbauer U, Della Bona A, Vichi A, Tholey MJ, Kelly JR, et al. ADM guidance—Ceramics: guidance to the use of fractography in failure analysis of brittle materials. Dent Mater. 2017;33(6):599–620. https://doi.org/10.1016/j.dental.2017.03.004
56. Ito C, Osada T, Ozaki S. Finite element analysis of fracture behavior in ceramics: competition between artificial notch and internal defects under three-point bending. Ceram Int. 2022;48(24):36460–68. https://doi.org/10.1016/j.ceramint.2022.08.206
57. Ramachandran N, Shetty DK. Rising crack-growth-resistance (R-curve) behavior of toughened alumina and silicon nitride. J Am Ceram Soc. 1991;74(10):2634–41. https://doi.org/10.1111/j.1151-2916.1991.tb06812.x
58. Kim Y-W, Mitomo M, Hirosaki N. R-curve behaviour and microstructure of sintered silicon nitride. J Mater Sci. 1995;30(20):5178–84. https://doi.org/10.1007/BF00356067
59. Nishida T, Hanaki Y, Nojima T, Pezzotti G. Measurement of rising R-curve behavior in toughened silicon nitride by stable crack propagation in bending. J Am Ceram Soc. 1995;78(11):3113–16. https://doi.org/10.1111/j.1151-2916.1995.tb09092.x
60. Fünfschilling S, Fett T, Hoffmann MJ, Oberacker R, Schwind T, Wippler J, et al. Mechanisms of toughening in silicon nitrides: the roles of crack bridging and microstructure. Acta Mater. 2011;59(10):3978–89. https://doi.org/10.1016/j.actamat.2011.03.023

## SUPPORTING INFORMATION

Additional supporting information can be found online in the Supporting Information section at the end of this article.

**How to cite this article:** Maeda T, Osada T, Ozaki S. Reliability evaluation scheme for ceramics based on defect size distribution inversely estimated from standardized tests. J Am Ceram Soc. 2025;108:e20660. https://doi.org/10.1111/jace.20660